CFD analysis of broaching for a model surface combatant with explicit simulation of moving rudders and rotating propellers

Pablo M. Carrica *, Hamid Sadat-Hosseini, Frederick Stern

IIHR – Hydroscience & Engineering, The University of Iowa, Iowa City, IA 52242, USA

ARTICLE INFO

ABSTRACT

The mechanisms of broaching in following regular waves are studied by analysis of free model computations. Simulations of the fully appended ONR Tumblehome model DTMB 5613 are performed with the ship hydrodynamics code CFDShip-Iowa v4.5 and validated against experiments of an auto-piloted, self propelled model ship. Appendages include bilge keels, skeg, shafts and struts, moving rudders to control heading, and rotating propellers for self-propulsion. Proportional and proportional–integral autopilots are used. Once validated against experimental data for the proportional controller, the flow field and forces and moments on the hull and individual appendages are analyzed in detail to identify the mechanisms leading to the broaching event. It was found that several reasons contribute to the inability of the ship to overcome the hydrostatic yaw moment caused by the approaching wave. However, it is shown that the use of a slightly better autopilot prevents broaching under identical operating conditions, presenting an opportunity to extend the safe operating envelope of the ship.

© 2011 Elsevier Ltd. All rights reserved.

1. Introduction

Loss of stability in a surface ship is a seriously dangerous condition that should be avoided at all costs. One of the most challenging loss of dynamic stability mechanisms is broaching, in which a ship cannot be steered and turns broadside to the waves, with large roll angles and violent accelerations. Model tests show that broaching usually happens in following or quartering waves with the ship advancing with a speed near the wave speed and with a target heading off from the wave direction, see for instance Umeda et al. [32]. However the processes leading to broaching events are more complex, resulting from a combination of hydrostatic forces caused by the waves, and dynamic forces arising from reactions by the propeller, hull, control surfaces and other appendages to the motions of the ship as discussed in Carrica et al. [8], who used the computational fluid dynamics (CFD) code CFDShip-Iowa v4.0 to study a broaching event for an ONR Tumblehome appended with rudders, skeg and bilge keels in irregular waves using a body-force propeller model. They found that strong hydrostatic yaw moments caused the turn of the ship, overwhelming the correcting moment induced by the rudders. The history of the trajectory and the controller played also an important role, potentially causing the rudders to be correcting in the wrong direction when the wave originating the broaching hits the ship.

Though several system-based and potential flow studies of stability and broaching can be found in the literature, see for instance Spyrou [28], Umeda et al. [31], Belenky et al. [1] and Yamamura et al. [37], CFD studies are scarce. CFD has the advantage of providing details of the physical processes involved on loss of stability events, enabling a deeper understanding of these processes that could be used to improve design, but it is considerably more expensive than system-based or potential flow approaches. For the ONR Tumblehome, Huang et al. [18] studied broaching in irregular waves, including the effects of air, and Sadat-Hosseini et al. [27] analyzed broaching in regular waves, comparing with data and system-based solutions. In their work, they also analyzed static maneuvers and evaluate the coefficients for the system-based model from CFD results. Extreme hurricane conditions, including wind loads, were simulated by Mousaviraad et al. [24].

With the advent of faster supercomputers and access to cheaper processing power, the use of moving appendages and propellers is slowly becoming popular. Simulation of free model problems requires the ability of provide self-propulsion and steering rudders, plus an autopilot or prescribed motions for more standard maneuvers like turning circles or zig-zags. Computation of maneuvers with rotating propellers and moving control surfaces has been pioneered by Pankajakshan et al. [26], who computed the radio controlled submarine ONR Body 1 using the code UNCLE with sliding grids for the propeller and interpolation between pre-generated grids for the deflection of the control surfaces. They performed a horizontal overshoot maneuver with results that compare well

---

* Corresponding author.
  E-mail address: pablo-carrica@uiowa.edu (P.M. Carrica).

with experimental data, showing improvements respect to body-force propeller model computations. Venkatesan and Clark [33] also performed computations of the ONR Body 1, simulating a horizontal overshoot maneuver with a sliding mesh to model the rotation of the propeller and deforming grids to simulate deflection of the control surfaces, showing good results but overpredicting the pitch angle and consequently the depth during maneuver. The computations by Pankajakshan et al. [26] and Venkatesan and Clark [33] were performed for deep maneuvers and thus neglected the presence of the free surface. Maneuvers for a KVLCC1 tanker with moving rudder and rotating propeller in a free surface flow have been reported by Carrica and Stern [9] using overset grids, for 35° rudder deflection turning circle and 20/20 zig-zag maneuvers. In addition to the described computations that use self-propulsion, computations with discretized rotating propellers have been performed for the KCS containership fixed at even keel attitude by Lübke [21] and Greve et al. [17] both using CFX, Bugalski and Hoffman [4] using StarCCM+, Wu et al. [35], Jin et al. [19] and Lee and Rhee [20] using Fluent, and for KCS free to sink and trim by Carrica et al. [12] using CFDShip-Iowa v4.5. The most comprehensive self-propulsion computations to date have been performed by Carrica et al. [10], who studied a tanker (KVLCC1 free to sink and trim) a containership (KCS fixed attitude) and a surface combatant (ONR Tumblehome free to sink and trim) using a speed controller to achieve self-propulsion and predict the propeller rotational speed. All those computations were performed at model scale, though KCS is extrapolated to ship point using ITTC procedures for the case fixed at even keel condition for all authors. Full scale self-propulsion computations have been performed by Castro et al. [13] for the KCS containership and compared with computations at model scale extrapolated to ship point.

In this paper CFDShip-Iowa v4.5 is used to analyze in detail a more controlled broaching process in following/quartering waves. The ship under study is the same ONR Tumblehome used by Carrica et al. [8], but fully appended with skeg, bilge keels, rudders with roots, shafts, struts and rotating propellers. The CFD case setup mimics the experimental conditions by Umeda et al. [32], which include a proportional heading controller and the propellers rotating at constant speed. Two conditions at $Fr = 0.4$ and $Fr = 0.45$ are compared against experimental data of pitch, roll, yaw and rudder angles for validation. Then the flow field and the forces and moments on the hull, propeller, rudders and appendages for the case with $Fr = 0.4$ are analyzed in detail in view of the processes leading to broaching. Finally, a proportional–integral controller with variable gain is tested, resulting in no loss of stability, demonstrating that a properly designed control system can dramatically extend the safe operating envelope of a ship. Since the study is performed using rotating discretized propellers, the computations are very expensive due to the large number of time steps required to properly resolve the flow around the propellers throughout the whole ship release, acceleration and broaching stages.

2. Modeling

Details of the mathematical and numerical models used in CFDShip-Iowa v4.5 are presented in detail elsewhere [7,11] and in the literature therein. A summary of the capabilities of the code are presented herein, with detailed discussion of the specifics pertaining to the simulations performed in this paper.

CFDShip-Iowa v4.5 solves the URANS equations using Menter [23] SST blended $k-\epsilon/k-\omega$ model for turbulence, with either integration to the wall or wall functions [2]. Detached eddy simulation (DES) is implemented based on Menter's SST model [30,36]. The free surface is modeled using a single-phase level set approach, in which the air/water interface is the zero level set of the level set distance function, with pressure Dirichlet conditions at the interface. Since the interface is embedded in the grid, an interpolation is used to impose the atmospheric pressure boundary condition [6]. The domain is discretized using multiblock/overset structured grids. The overset capabilities are fully dynamic, which allows the code to simulate large-amplitude motions. The overset connectivity is obtained at run time using the code Suggar [25]. Spatial terms are approximated with finite differences second-order upwind (for RANS) or fourth-order upwind biased (for DES) discretization of the convection terms and second-order centered scheme for the viscous terms. The temporal terms are discretized using a second-order backwards Euler scheme. Incompressibility is enforced by a strong pressure/velocity coupling, achieved using either PISO or projection algorithms. The equations of motion are solved only on the water side, while quantities are extended into the air to satisfy the proper boundary conditions at the interface. Regular and irregular, long or short crested waves are implemented through initial and boundary conditions, with Bretschneider, JONSWAP and Pierson-Moskowitz spectrums. Propellers are modeled either using a simple actuator disk/body-force approach in which local velocity effects on the propellers are neglected [29] or by fully discretizing the propellers including blades and hub. 6DOF capabilities are implemented using Euler angles [16], and enabled with a hierarchy of bodies. The ship (parent object) and appendages move together respect to static grids, while rudders, propellers and control surfaces follow the ship but can have their own motion relative to it (children objects). At this point, the children objects are considered massless, i.e. the moments of inertia and center of gravity location do not change when they move, and there are no reactions induced by this motion. The fluid flow equations are solved in an earth-fixed inertial reference system, while the rigid body equations are solved in the ship system, so forces and moments are projected appropriately to perform the integration of the rigid body equations of motion, which are solved iteratively. Feedback controllers are used for heading and speed control, while open loop controllers are used for maneuvers. In this paper, proportional–integral (PI) controllers [16] of the form

$$a = Pe + I \int_0^t e\,dt \tag{1}$$

are used, where a is the controller output, P and I are the proportional and integral gains, respectively, and e is the error respect to the target value. For speed and heading, these errors are defined as

$$e_U = U_{target} - U_{ship} \tag{2}$$

$$e_\psi = \psi_{target} - \psi \tag{3}$$

with ψ the yaw angle. The controller output in case of a speed controller is n, the propeller rotational speed in revolutions per second (RPS). In case of the heading the action is δ, the rudder angle.

3. Geometry

The model under consideration is the DTMB model 5613, named the ONR Tumblehome. The ONR Tumblehome is the research version of the US Navy surface combatant DDG-1000 Zumwalt class. Views of the ship model are shown in Fig. 1, with main particulars listed in Table 1. The reference ship system follows the customary CFD standard, with x the longitudinal axis pointing to stern, y pointing to starboard and z pointing upwards with $z = 0$ at the calm water plane. The earth system is coincident with the ship system at rest and is denoted by (X_e, Y_e, Z_e). The model is appended with bilge keels, skeg, shafts and struts, and includes the superstructure and a flight deck. Twin rudders with trunk root are included to steer the ship. Propulsion is provided by twin counter rotating propellers, inboard on top. The propellers
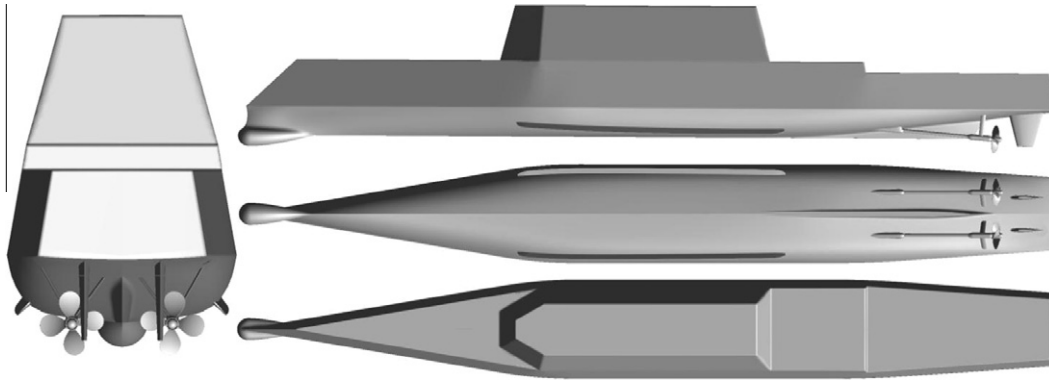
Fig. 1. ONR-Tumblehome model DTMB 5613 geometry, coordinate system, and motions definitions.

Table 1
ONR-Tumblehome model DTMB 5613 main particulars.

	Ship	Model		Ship	Model
Length: L	154.0 m	3.147 m	Meta-centric height: GM	2.068 m	0.0423 m
Breadth: B	18.78 m	0.384 m			
Draft: T	5.494 m	0.112 m	Roll radii of gyration: k_x/L	0.054	0.054
Displacement: m	8507 ton	72.6 kg			
Block coefficient: C_b	0.535	0.535	Pitch and yaw radius of gyration:k_y/L and k_z/L	0.25	0.246
Longitudinal position of centre of gravity from midship: x_{CG}	2.587 m aft	0.053 m aft			
Maximum rudder angle: δ_{MAX}	±35°	±35°	Rudder area: A_R	28.639 $m^2 \times 2$	$0.012 m^2 \times 2$

are 4-bladed with almost symmetric blade design. The roll restoring moment for the model in a similar configuration (but not exactly the same) has been presented by Carrica et al. [8], and exhibits a sharp increase beyond 65° roll, making capsizing virtually impossible. This is due to the immersion of the superstructure. In addition, the restoring moment is essentially constant for roll angles between 36° and 53°.

4. Grid system

The overset grid system consists of independent grids for hull, appendages, propellers, rudders, refinements and background, for a total of 49 blocks distributed to 190 processors. The grid spacing in the first grid point away from the solid surfaces was selected so that $y^+ \leqslant 1$, as required by the $k–\epsilon/k–\omega$ turbulence model. The basic geometry was generated using mostly hyperbolic extrusion on the starboard side, and then the grids were mirrored to obtain the port grids. Then global grids spanning both sides were constructed. Table 2 summarizes the grid system used, depicted in Fig. 2 during an instant of a broaching event. For the starboard side, the hull is discretized using a double-O grid with poles located in the centerplane by the sonar dome and near the end of the skeg on the stern. The superstructure overlaps the hull and has wrapped topology with $j = 1$ on the solid surface. In order to allow for the propellers to rotate, a ring gap is left between the shaft and the propeller hub, which is discretized using a double O topology. Each of the 4 propeller blades overlap the hub and are attached rigidly to it. Grids are wrapped around the tips of the blades to form a watertight system and provide high resolution for the tip vortices and air entrained through the free surface.

In the case of the rudders, realistically spaced gaps are left between the roots and the rudder spades. This is possible thanks to the gaps being perfectly horizontal, and thus aligned with the Cartesian octree used by Suggar to define the hole cutting approximation. Once the grid is generated and static overset connectivity information is obtained with Suggar, the weights necessary to compute forces, moments and areas accounting for overlapping panels on solid surfaces are calculated using the code Usurp [3].

5. Experimental and simulation conditions

The experimental conditions are followed as closely as possible in the simulations, and summarized in Table 3. In all three cases, following waves are imposed while the ship controller attempts to steer the ship with a set angle respect to the direction of the waves. The wavelength and amplitude of the waves for all cases are $\lambda/L = 1.25$ and $a/L = 0.03125$, respectively, corresponding to amplitudes of sea state 7 in full scale. Experimental data for pitch, roll, yaw and rudder action exists for Cases 1 and 2 [27], which differ in heading angle and ship speed. For these cases the heading controller is purely proportional (P) with unit gain. These two cases have been used to validate the computations. Due to the high cost per run, verification was not attempted.

Mimicking the experimental procedures, all cases are run with constant propeller RPS. The rotational speed of the propellers is set to that obtained by self-propulsion at the corresponding Froude number. Self-propulsion computations with speed controllers [10] are used to find the RPS at the corresponding Froude numbers, as listed in Table 3. For all cases the rudder rotation rate is limited to the experimental value of 23.4° per second.

Notice that no cavitation or ventilation models are implemented for these computations. Cavitation, though extremely important for a broaching process in full scale, should be negligible in model scale. Ventilation is a complex phenomenon that draws air from the free surface into the propeller. Califano and Steen [5] found that RANS simulations of a highly loaded ventilating

Table 2
Simulation grid details.

Name	Size (grid points)	# of Procs	Type
Hull S/P[a]	$199 \times 61 \times 104$ (1.26 M $\times$ 2)	12 ($\times$2)	Double O
Skeg S/P	$61 \times 49 \times 40$ (0.12 M $\times$ 2)	1($\times$2)	O
Bilge Keel S/P	$99 \times 45 \times 50$ (0.23 M $\times$ 2)	2($\times$2)	H
Rudder Root Collar S/P	$121 \times 35 \times 28$ (0.12 M $\times$ 2)	1($\times$2)	O
Rudder Root Gap S/P	$121 \times 51 \times 19$ (0.12 M $\times$ 2)	2($\times$2)	Conformal to Collar
Rudder Outer S/P	$61 \times 36 \times 55$ (0.12 M $\times$ 2)	1($\times$2)	Double O
Rudder Inner S/P	$61 \times 36 \times 55$ (0.12 M $\times$ 2)	1($\times$2)	Double O
Rudder Gap S/P	$121 \times 51 \times 19$ (0.12 M $\times$ 2)	2($\times$2)	Conformal to Inner and Outer
Shaft Collar S/P	$39 \times 50 \times 57$ (0.11 M $\times$ 2)	1($\times$2)	O
Shaft Proper S/P	$74 \times 41 \times 37$ (0.11 M $\times$ 2)	1($\times$2)	O
Shaft Tip S/P	$110 \times 117 \times 100$ (1.29 M $\times$ 2)	12($\times$2)	O with end pole
Strut Outer S/P	$69 \times 34 \times 50$ (0.12 M $\times$ 2)	1($\times$2)	O
Strut Inner S/P	$69 \times 34 \times 50$ (0.12 M $\times$ 2)	1($\times$2)	O
Propeller Hub S/P	$118 \times 44 \times 61$ (0.32 M $\times$ 2)	3($\times$2)	Double O
Propeller Blades 1–4 S/P	$4 \times 62 \times 40 \times 97$ (4 $\times$ 0.24 M $\times$ 2)	4×2 ($\times$2)	O
Propeller Tips 1–4 S/P	$4 \times 58 \times 41 \times 51$ (4 $\times$ 0.12 M $\times$ 2)	4×1 $\times$(x2)	Wrap
Propeller Refinement S/P	$124 \times 61 \times 185$ (1.4 M $\times$ 2)	12 ($\times$2)	O
Superstructure	$165 \times 61 \times 85$ (0.86 M)	8	Wrap
Refinement Stern Region	$229 \times 161 \times 112$ (4.13 M)	36	Cartesian
Background	$217 \times 103 \times 83$ (1.86 M)	16	
Total	(21.1 M)	190	

[a] S/P: Starboard/Port.
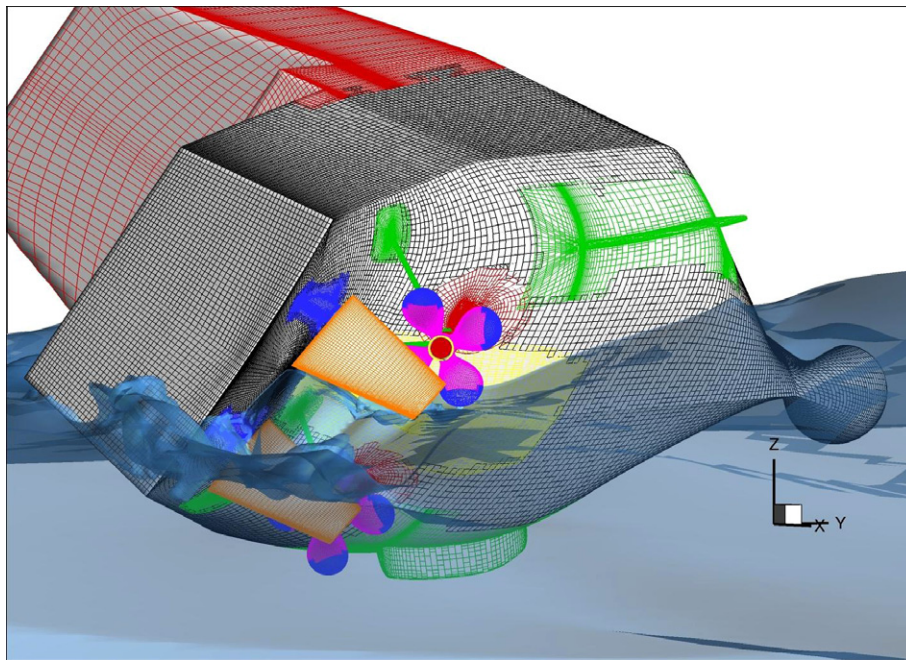
Fig. 2. Overset grid system and instantaneous view of the free surface.

Table 3
Details of the simulation cases.

	Exp. data	Fr	n (RPS)	Wavelength, λ/L	Wave amplitude, a/L	Heading target respect to waves (degrees)	Proportional gain, P	Integral gain, I	Max rudder rate (degrees per second)
Case1	Yes	0.4	18.92	1.25	0.03125	22.5	1	0	23.4
Case 2	Yes	0.45	21.52	1.25	0.03125	30	1	0	23.4
Case 3	No	0.4	18.92	1.25	0.03125	22.5	3–5 variable	2–0.75 variable	23.4

propeller ($J = 0.1$) show satisfactory prediction of thrust and torque for the blades coming downward from the free surface but poorer predictions for the blades approaching the free surface from below. The authors fault the poor predictions on the second half of the

revolution to the grids being too coarse with 2.35 million cells for the whole domain including the 4-bladed propeller, preventing the entrained air cavities from reaching beyond the first half of the propeller. Each propeller in this work has about 3.2 million

points, more than twice the grid density of Califano and Steen [5] in the propeller proper. Ventilation on a propeller near or across a free surface is an active area of research, and though CFD computations have shown results with adequate trends there still much work needed in the subject. This is particularly true in terms of ventilation at full scale, since the Weber number is very different compared to model scale, where most of the experimental data is currently available.

Case 3 was chosen as a demonstration that a better controller can extend the safe operating envelope of the ship. In this case the conditions are identical to those of Case 1, but a PI controller with variable gain is used. Details are discussed later in section "PI controller."

The initial conditions of pitch, roll, yaw and rudder action are known from the experimental data. Initial conditions for wave phase, ship speed, and heave are unknown and were estimated using a simple propeller body force model, using trial and error runs until the data for the first few seconds of simulation was reasonably matched [27].

Reference speed $U_0 = 2.778$ m/s and ship length $L_0 = 3.147$ m were used to non-dimensionalize the problem, corresponding to a Froude number $Fr = 0.5$. The dimensionless time step was set to $\Delta t = 0.00025$, resulting in approximately 1.9° of propeller rotation per time step. All computations were performed using DES turbulence modeling. Computations took around 30,000 time steps to complete. Since the time step is very small, an explicit scheme was used for the computation of the predicted motions. Five Suggar groups each running in one processor in lagged mode [11] were used to compute the domain connectivity information, which adding to the 190 processors used by the CFD solver results in a 195 processor run. The computations were performed in an SGI Altix 4700, taking approximately 4 weeks of wall clock time.

6. Validation

This section concentrates in the cases with proportional controller, for which there is data available. A verification study has been performed for a much simpler geometry of ONR Tumblehome (appended only with bilge keels) with no propellers, shafts, struts, rudders or rudder roots [27]. The study was carried out at model scale for a range of forward speeds, free to sink and trim, and with 10° of heel angle to investigate the grid convergence not only for resistance and sinkage and trim but also for side forces and roll and yaw moments which are significantly important in complicated cases such as broaching. The overall conclusion was that the ship motions, forces and moments were fairly insensitive to grid changes. For a fully appended model with discretized rotating propellers in a broaching event, a grid study is an extremely costly process.

Since the grids have been designed for optimal overlap and maximizing computational efficiency, they cannot be coarsened significantly while maintaining enough overlap to obtain a valid interpolation throughout the whole computation. Coarsening the overall grid by a factor of $\sqrt{2}$ yields orphans in several appendages, including the shafts and rudders near the hull. Orphan points appear when an interpolated point is needed but there are no donor grids with enough active points available; valid donor cells must have majority of active points. This is because as the grids get coarser the overlap decreases, but still two valid fringe points are needed to obtain a valid overset interpolation, see Carrica et al. [11] and references therein for details of the requirements resulting from overset grids in problems with motions.

Since only finer grids can be used for a verification study in this case, en estimation of the cost of performing such study is provided. Using a $\sqrt{2}$ refinement ratio (probably the smallest acceptable for a verification study) would lead to 59.67 and 168.7 million points for the medium and fine grids, respectively. The number of CPU hours would be approximately 320,000 and 880,000, requiring respectively 600 and 1650 processors. This compares with about 300,000 CPU hours used in total for all computations performed herein. Therefore, a grid convergence investigation multiplies the cost of this study by a factor of 5. In addition, time step studies would further increase the cost, since at least one time step has to be smaller than the one chosen herein to prevent points from changing from blanked to active in two consecutive time steps [7, p. 1420]. Performing the time step study in the grid used in this paper would add another 250,000 CPU hours, increasing the cost of the overall study performed in this paper by a factor of approximately 6.

Though cost is the main factor that prevented the authors from performing a verification study, other issues are important as well. Celik et al. [14,15] argue that refined grids in DES computations resolve more physics and make it harder to achieve asymptotic behavior in a grid study, questioning the validity of applying Richardson extrapolation to these type of computations. Additionally, highly complex transient simulations like those performed in this paper do not have a clear predicted quantity that can be used for the verification study, as all change in time. This would further complicate the evaluation of the uncertainty of a given variable. For instance, if the roll angle is chosen for verification, problems may arise if the different grids predict broaching at different times, making it difficult to compare the roll angle between grids at a given stage of the broaching process. Comprising a high effort research undertaking in itself, a complete verification study for the broaching process with complex grids and motions as described in this paper is left as future work.

Fig. 3 shows experimental data and CFD results of roll, pitch, yaw and rudder angles for Case 1. CFD results of the drift angle, Froude number (ship speed) and trajectory are also presented. CFD results are shown for discretized propeller with P (Case 1) and PI (Case 3) controllers and for non-interactive body-force propeller model with conditions identical to Case 1 [27].

The broaching process occurs as a large wave approaches the ship from the stern, pushes the ship forward, at the same time creating a strong yaw moment broadside to the wave. The ship accelerates and turns rapidly unable to overcome the hydrostatic yaw moment imposed by the wave until finally broaches with a large roll excursion. The process can be seen clearly in Electronic Annexes I and II, which show animations for Cases I and II at 50% real time (thus 2 s in the animations correspond to 1 s in the figures). Notice that the use of a small number of frames per second causes aliasing and gives the illusion of the propeller rotating slowly and outboard on top, while in reality it is rotating inboard on top at about 20 RPS, see Table 3.

The following description concentrates in the case with P controller, for which the data corresponds. The ship is released with a heading of about −5°, pitch angle around −1° and very small roll angle to port, see Fig. 3. The rudders start immediately to correct to the target heading of – 22.5° by turning to starboard. The yaw rate increases rapidly, and so does the roll angle to reach a peak of about 60°. The broaching occurs approximately at 6 s after release, where the yaw rate is maximum and the roll experiences an excursion with maximum roll rate. The wave passes the ship shortly after at around 7 s, this evident by the bow up pitch motion between 7 and 9 s. The yaw angle reaches 78° in the experiments, and about 69° for CFD for both body force and discretized propeller approaches. Since the heading controller gain is $P = 1$, for yaw angle above 52.5° to starboard (30° or more of error respect to the target heading) the rudders turn hard to port, but are unable to correct the course. The ship experiences initially a speed reduction to a Froude number of about 0.4 at 1.5 s. The wave reaches the ship
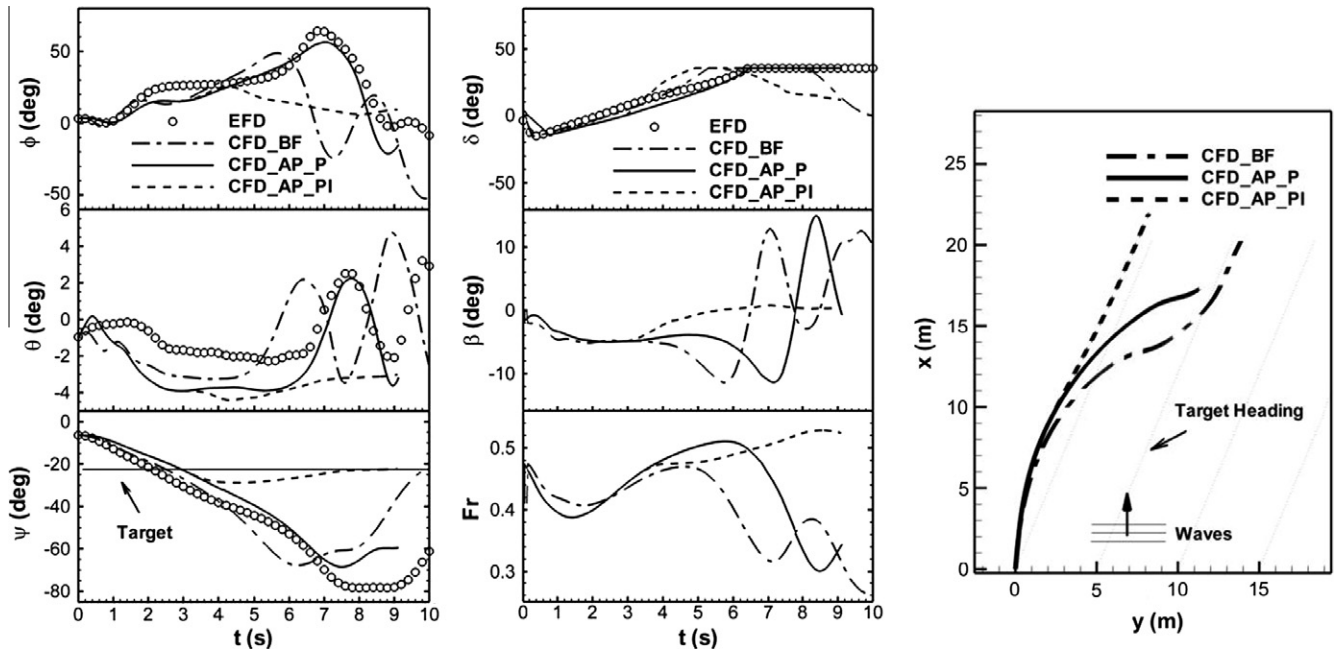
Fig. 3. Roll, pitch and yaw angles (left), rudder angle, drift angle and Froude number (center), and ship trajectory (right) for Cases 1 and 3. BF and AP stand for "Body Force" and "Actual Propeller," respectively, while P and PI are proportional and proportional–integral controllers. Case 1 corresponds then to AP_P and Case 3 to AP_PI.

approximately at that time and the ship starts surf riding the wave, with the Froude number reaching 0.5 immediately before the broaching event, see also the pitch angle showing that the bow dips as the ship surfs the wave. Overall the simulation with the discretized propeller shows very good agreement with the experimental data, and much better results than those with the body force model. The roll history and amplitude are very well predicted, as well as the rudder action and time of occurrence of the peaks of pitch and yaw. The weakest predicted parameter is the pitch angle during the surf-riding phase of the broaching process, overestimated by over 50% of the bow down angle. The reason for this difference is not clear, but could be due to differences in static trimming.

Comparisons with data for Case 2 are shown in Fig. 4. This case is more severe because the target angle respect to the waves is 7.5° larger than for Case 1, resulting in larger hydrostatic yaw moments caused by the waves. The agreement with the experimental data is very good for all variables. The broaching process is similar to Case 1, but due to more instable nature of the broaching process it happens earlier after release of the ship. Though the body force computations show better agreement than for the previous case, the discretized propeller results are still clearly superior. The time history of heading follows the experimental data very well, as does the roll history. The pitch history is closer to the experiment than it was for Case 1, though it still exhibits the poorest fit with the data. The amplitudes and phases of the three bow up events at 2,
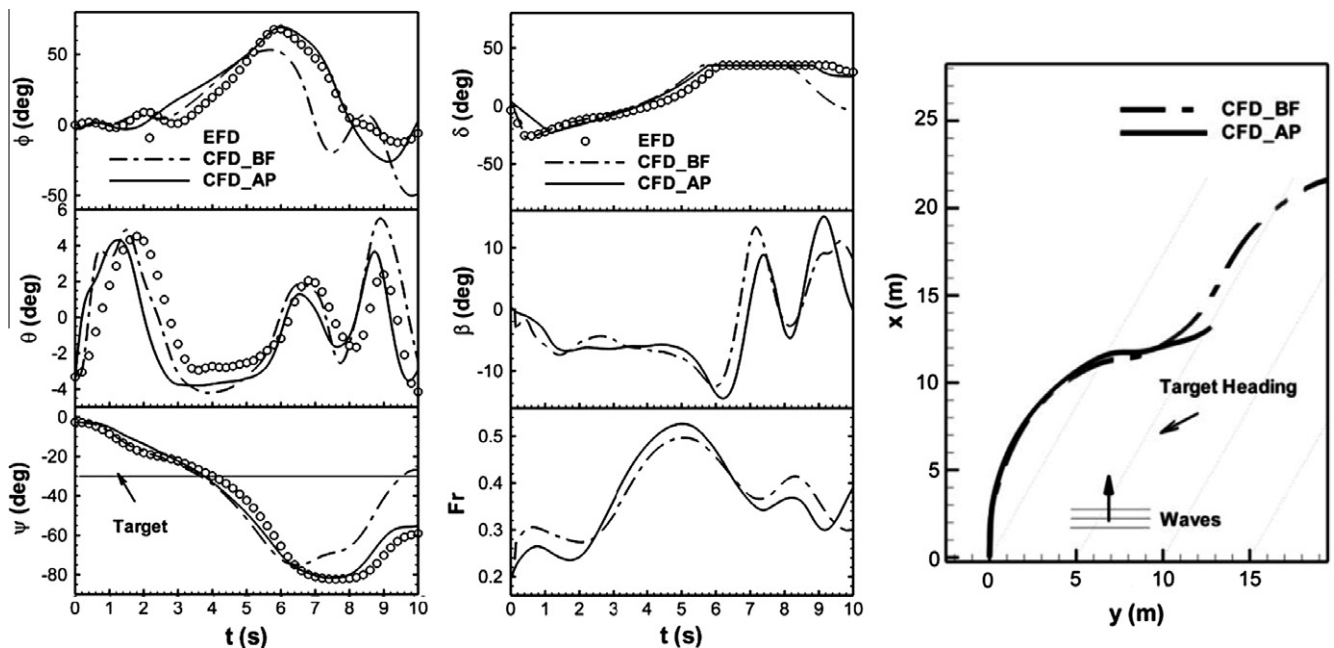

Fig. 4. Same as in Fig. 3 but for Case 2.

7 and 9 s are well predicted, but the bow down ride during the broaching is still overpredicted, but to a less extent in Case 1.

In both cases the wave celerity is V_c = 2.478 m/s, corresponding to Fr = 0.446. In Cases 1 and 2 the speed exceeds Fr = 0.5 during the surf riding leading to broaching, to slow down considerably after broaching as the wave overcomes the ship and the rudders try to take the ship back to target heading. Figs. 3 and 4 also show the trajectories of the two broaching events, where it is clear that as the ship deviates considerably from the target heading it also follows an erratic trajectory. Notice in the trajectory for Case 2 with body force model, that the ship achieves the target heading again after the broaching event, but with a velocity that is much lower than the wave celerity, resulting in the next waves reaching the ship and causing a second broaching event.

Fig. 5 shows instantaneous views of the broaching process for Case 1, with vortical structures depicted as isosurfaces of the second invariant of the rate of strain tensor Q = 500. The isosurfaces of Q are colored with axial velocity. The interaction of the propellers' tip and hub vortices with the rudders is remarkable even when the propellers are partially submerged. The free surface responds to the presence of the propeller vortices (this can be clearly seen in Fig. 5 upper-left). An animation of Fig. 5 slowed to 10% of the normal speed is shown in Electronic Annex III.

The complexity of the flow is further shown in Fig. 6, which illustrates the magnitude of Q on axial cross sections along the hull at t = 7.1 s. Vortices detaching from the sonar dome and the bilge keel evolve smoothly until they reach the propeller plane, where they are shattered by the propellers. The port bilge keel exhibits a very strong vortex, created by the strong drift to port. This vortex points mostly to the stern, with a large positive streamwise component, and hits the port propeller almost on its axis. This vortex can also be seen in Fig. 5 on the upper-right. Vortices originating from the propeller shaft and struts are shed periodically and also interact with the propeller and rudders.

7. Forces and moments

Dimensional forces and moments in the ship system of reference for the rudders, propellers, and the whole ship for Cases 1 and 2 are shown in Figs. 5 and 6, respectively. The forces (X, Y, Z) and moments (K, M, N) on the ship are separated into hydrostatic, dynamic pressure and friction. These are first calculated in dimensionless form in the Earth coordinate system, where the flow equations are solved

$$F_e = \int_S \left[\left(\frac{\nabla \boldsymbol{u} + \nabla \boldsymbol{u}^{\mathsf{T}}}{2Re} \right) - \left(p - \frac{z}{Fr^2} \right) \boldsymbol{I} \right] \cdot d\boldsymbol{a}_e \tag{4}$$

$$L_e = \int_S \boldsymbol{r} \times \left\{ \left[\left(\frac{\nabla \boldsymbol{u} + \nabla \boldsymbol{u}^{\mathsf{T}}}{2Re} \right) - \left(p - \frac{z}{Fr^2} \right) \boldsymbol{I} \right] \cdot d\boldsymbol{a}_e \right\} \tag{5}$$

where $\boldsymbol{u}$ is the local velocity vector, p is the pressure and $\boldsymbol{r}$ is the vector from the ship's center of gravity to the surface point. The forces and moments are then projected into the ship system to yield

$$F^* = (X^*, Y^*, Z^*) = \boldsymbol{J}^{-1} F_e \tag{6}$$

$$L^* = (K^*, M^*, N^*) = \boldsymbol{J}^{-1} L_e \tag{7}$$

where $\boldsymbol{J}$ is the transformation matrix relating vectors in the ship system with vectors in the Earth system [16]. The dimensional forces and moments are obtained from
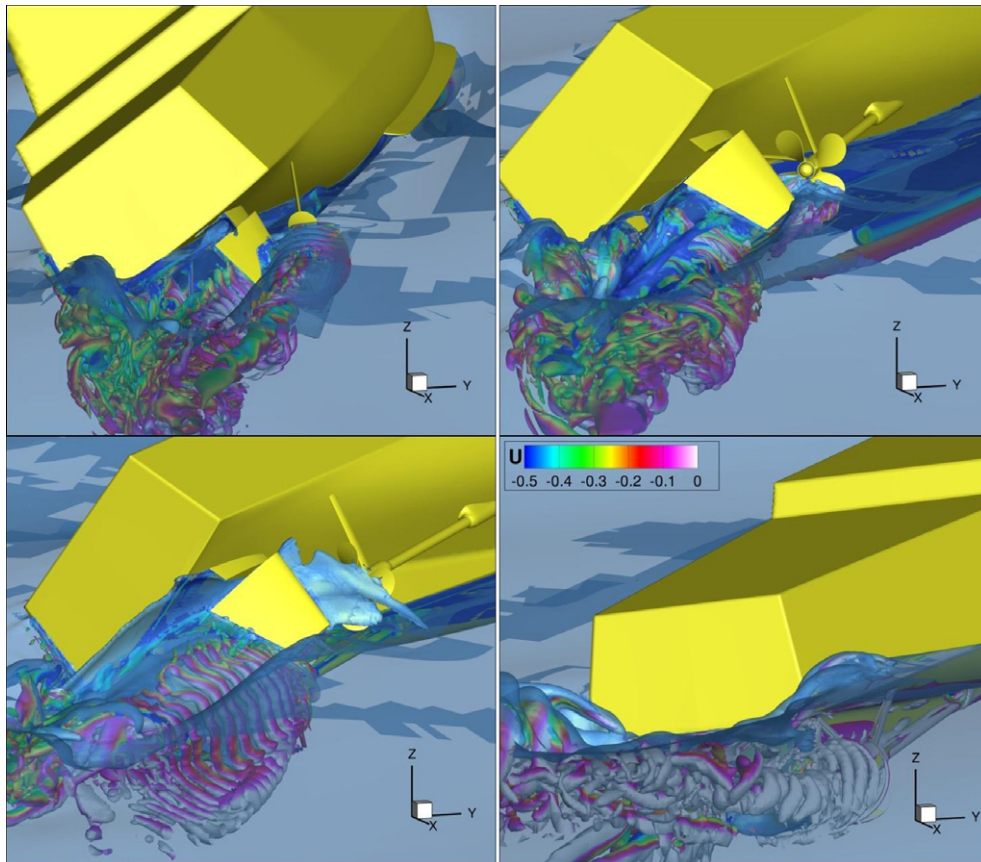

Fig. 5. Instantaneous views of the broaching process for Case 1. Vortical structures are shown as isosurfaces of Q = 500. Upper-left: t = 5.66 s, upper-right: t = 6.51 s, lower-left: t = 7.27 s, lower-right: t = 8.21 s.
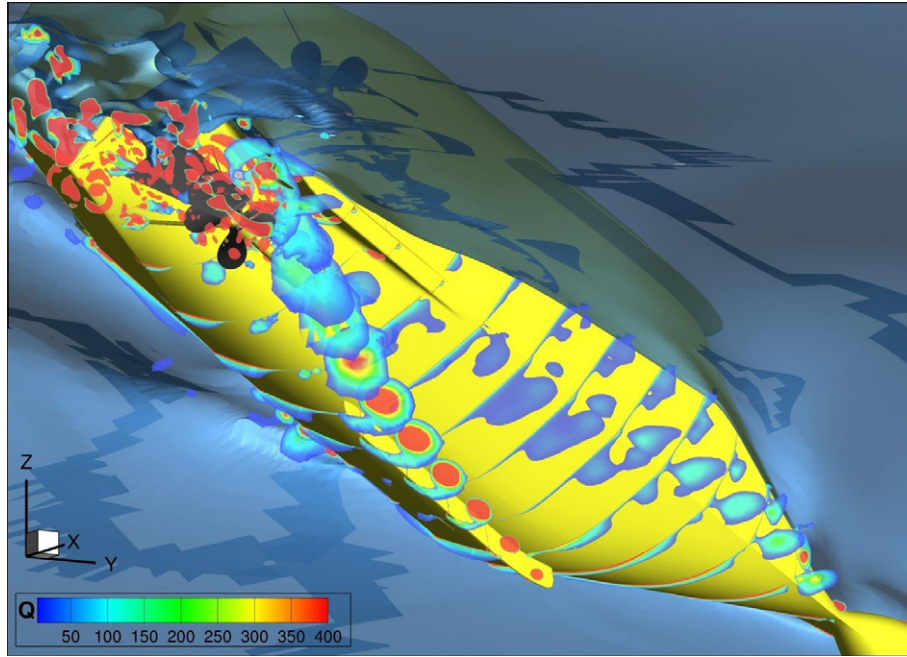
Fig. 6. Instantaneous axial cross sections showing vortical structures represented by Q at t = 7.1 s.

$$\boldsymbol{F} = (X, Y, Z) = \frac{1}{2}\rho U_0^2 A_w \boldsymbol{F}^* \tag{8}$$

$$\boldsymbol{L} = (K, L, M) = \frac{1}{2}\rho U_0^2 L_0 A_w \boldsymbol{F}^* \tag{9}$$

where A_w is the instantaneous wetted area.

8. Global forces and moments

Forces and moments for the complete ship (including appendages and propeller) and for the rudders and propellers are shown in Fig. 7 for Case 1. The hydrodynamic surge, sway and heave forces are decomposed in their friction and pressure components, and the weight is also shown. The surge exhibits a strong gravitational force as the wave causes the ship to pitch bow down, causing a stage of surf riding (recall that negative force corresponds to a forward thrust). During this stage of surf riding (from 2 to 6 s) the magnitude of the wave force is 50–100% larger than the thrust of the propellers. During broaching the wave overcomes the ship, the starboard propeller and rudder come out of the water, and the gravitational forces reverses. Right before the starboard rudder comes partially out of the water, the rudders' resistance is larger than the thrust from the propellers, and stays very large even as propeller and rudder come back into the water at the end of the broaching process. This is a consequence of the autopilot turning the rudders all the way to port trying to take the ship back on course (see Fig. 3). As soon as the starboard propeller gets back in the water the thrust almost duplicates to reach about 40 N, 30% more than the thrust before the broaching started. This is due to the much lower ship velocity at this stage, which results in a lower advance coefficient in the propellers and higher loads.

The roll moment K in Fig. 7 is mostly dominated by the rudders. As the wave pressure forces create a negative yaw moment that turns the ship to starboard, the rudders react compensating with a positive yaw moment by turning to port. This causes a large rolling moment that reaches in excess of 5 Nm. The restoring moment for this ship stays around 5 Nm from 25° to 60° of roll [8], thus making the rudders very significant contributors to the large roll excursion observed during broaching. Notice also that the propel-

lers contribute another 1 Nm to the roll moment, exacerbating the problem. In addition, the rudders contribute about 30 N of sway force to starboard, but mostly pressure on the hull balances the very large side force during broaching. The propellers contribute in excess of 10 N of vertical force during periods of maximum load, a considerable amount for a model ship weighing 712 N.

The forces and moments for Case 2 show similar trends, but the numbers are more dramatic and the initial conditions differ significantly, see Fig. 8. Since the initial velocity is lower than for Case 1 (Fr = 0.2 for Case 2 vs. Fr = 0.45 for Case 1), the propellers are heavily loaded and they account for most of the surge pressure force. As the ship accelerates the load on the propellers decreases and the ship resistance increases, leading to a balance of surge forces. From 2 to 6 s the gravitational force is very large and helps push the ship as it broaches. As in Case 1, the rudders are large contributors to the overall resistance and the roll moment.

9. Loads on the propellers

The loads on the propellers are better described on the shaft system of coordinates, which is not aligned with the ship system of coordinates, see Fig. 1. In this system x points forward in the direction of the shaft, y points to starboard (this in coincidence with the ship system of coordinates) and z is normal to x and y forming a right-hand system. Thus a positive thrust pushes the shaft forward and a positive torque follows the right hand rule on a vector aligned with the shaft pointing forward.

Fig. 9 shows thrust, torque, side force (in the y direction) and yaw moment (around z) for starboard and port propellers. Both propellers start with about the same magnitude of thrust, but as the ship turns to starboard and rolls to port the thrust developed by the starboard propeller decreases, while the thrust on the port propeller stays essentially constant. There are three important effects present that tend to reduce the thrust on the starboard side. First, note in Fig. 3 that the ship speed increases steadily from 1 s to 6 s, thus causing an increase on the advance velocity at the propeller suction side, in consequence reducing the thrust coefficient. Second, as the ship rolls (see once again Fig. 3) the starboard pro-
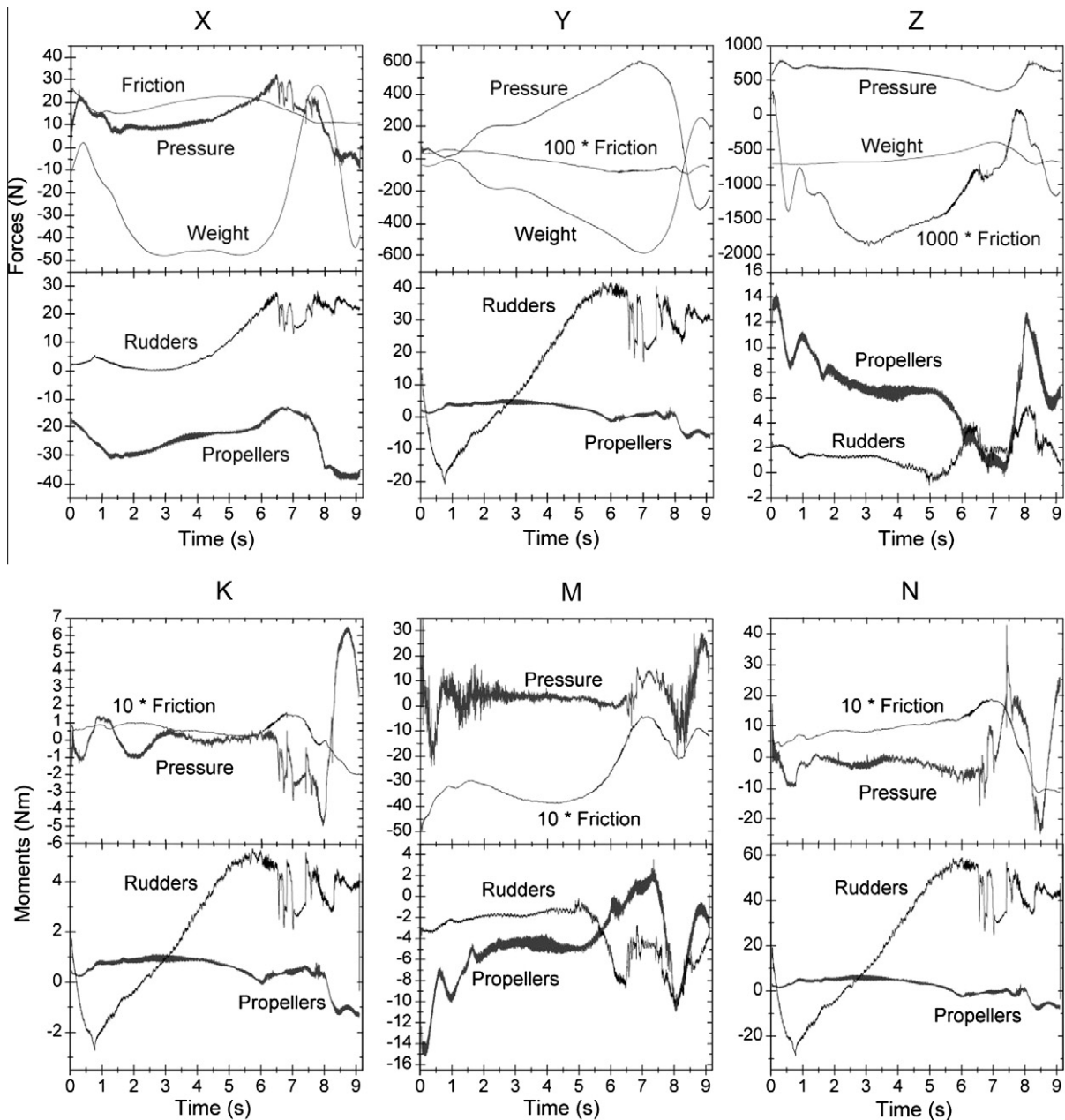
Fig. 7. Forces (top) in x (left), y (center) and z (right), and moments (bottom) around x (left), y (center) and z (right) for Case 1.

peller gets closer to the free surface, also reducing the thrust. The acceleration of the ship affects a lot less the thrust on the port propeller, decreasing slightly between 1 s and 3.5 s, when the ship acceleration is largest, and staying mostly constant from 3.5 to 6.5 s, where changes in ship speed are more moderate. A third effect that tends to decrease the thrust of the starboard is caused by the drift velocity. In this case the drift velocity is from port to starboard in the ship system of coordinates, hindering the starboard propeller as the rotation of the propellers is inboard on top. The drift angle is shown in Fig. 3, and drift velocities are largest at the stern. Large drift velocities cause the generation of the bilge keel vortex that hits the port propeller rotating in the opposite direction to the propeller, tending to increase its thrust.

As the starboard propeller gets out of the water the thrust decreases rapidly and the forces and moments are as expected more unstable. For about a second between 6.5 s and 7.5 s the propeller is mostly out of the water and produces essentially no thrust or

torque, see also Fig. 5. As the ship recovers from the roll excursion and the starboard propeller gets back in the water with the ship advancing at low speed, the thrust recovers and peaks at about 20 N, with the torque also reaching maximum values.

The side force is essentially positive for both propellers during the first half of the computation, and significantly larger for the port propeller. This supports the hypothesis that the drift velocity plays an important role on the performance of the propellers. A drift velocity from port to starboard increases the load on the lower blades of the port propeller, with the opposite effect on the starboard propeller (remember the rotation is inboard on top). A decrease of the load will be observed on the upper blades of the port propeller, and *vice versa* for the starboard propeller, but since the advance velocity is smaller near the hull the effect will be smaller. Though relatively small compared to the rudder moments (see Fig. 7), the propeller side forces and resulting yaw moments can have considerable effects on maneuvering.
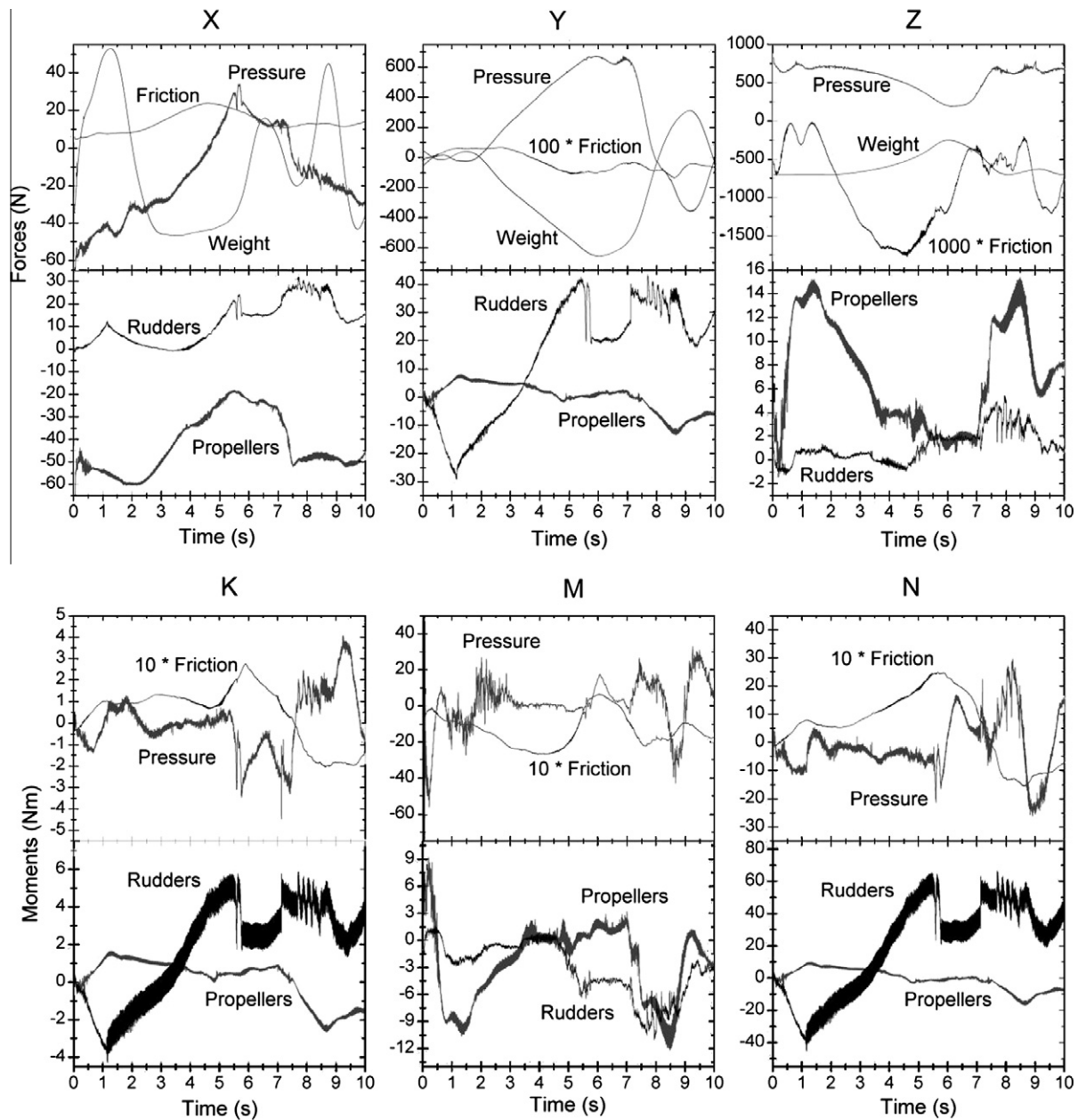
Fig. 8. Forces (top) in *x* (left), *y* (center) and *z* (right), and moments (bottom) around *x* (left), *y* (center) and *z* (right) for Case 2.

Another interesting feature clear from Fig. 9 is the presence of low frequency fluctuations on forces and moments on the propellers. These are probably caused by vortices shed periodically by the struts and the shafts, which are captured by the propellers. These vortices are clearly shown in the animation from Carrica et al. [10], Supplemental Material 2, which depicts a view from below of the self-propulsion point at *Fr* = 0.4, the same as Case 1.

Thrust and torque developed by a single blade of the propeller at four different times during the computation of Case 1 are shown in Fig. 10. The starboard blades suffer much higher thrust and torque fluctuations due to a more non-uniform nominal wake velocity, caused in part by the starboard propeller being downstream of the hull respect to the drift velocity, and in part by the presence of the free surface. Fig. 11 shows axial velocities (in the ship's reference frame) at an axial plane immediately upstream of the propellers and downstream of the supporting struts at 4, 6 and 8 s.

At 4 s the amplitudes of thrust and torque fluctuations for the starboard propeller blade are almost twice the values for the port

propeller blade, see Fig. 10. This is caused by the much less uniform inflow to the starboard propeller than to the port one, as depicted in Fig. 11, where the upper half of the starboard propeller sees axial velocities below 0.75, while the lower half is exposed to axial velocities near 0.95, resulting in a peak-to-peak thrust fluctuation amplitude of 3.6 N. The port propeller blade, on the other hand, is never subject to inflow axial velocities above 0.9 or below 0.6, with consequent peak-to-peak fluctuation of thrust of 1.8 N, half the amplitude of the starboard propeller blade. A large intrusion of slower moving flow is observed in Fig. 11, essentially covering the port propeller, caused by the bilge keel vortex discussed earlier. As the roll angle and velocity increase this vortex becomes more energetic, as shown in Fig. 11 for 6 s. At this time the ship is moving very fast (*Fr* = 0.51, see Fig. 3), and the starboard propeller comes partially out of the water, and presents large thrust and torque fluctuations as the blade interacts with the free surface, resulting effectively in zero thrust and torque when the whole blade leaves the water. Conversely, the port propeller blade is exposed
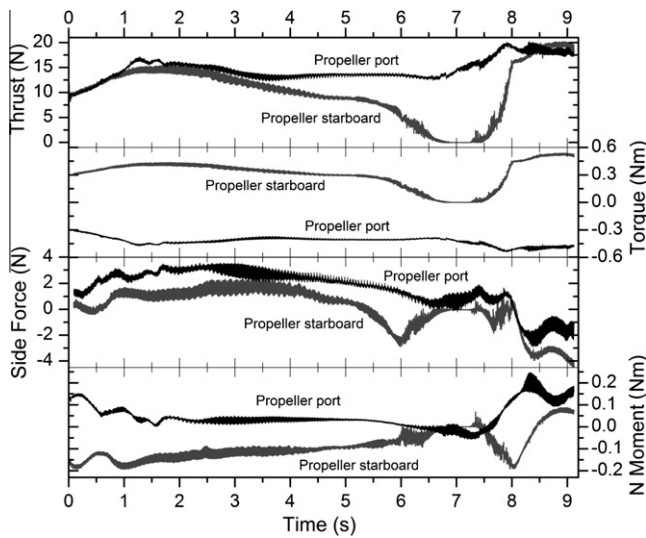
Fig. 9. Thrust, torque, side force and yaw moment on the reference frame of both propellers for Case 1.

expected, the main frequency is coincident with the propeller rotating frequency of 18.92 Hz. Higher harmonics of decreasing amplitude are present for both propellers. Consistent with the analysis of Fig. 10, for all time intervals the amplitude of the fluctuations is higher for the starboard blade than for the port blade. An exception to this is the second harmonic at the interval between 3 and 4 s, where the port blade shows more amplitude. This is also consistent with Fig. 10, where the port blade exhibits a clear smaller peak at every through. The reason for this small peak is a significant upward velocity, caused by the bilge keel vortex, that increases the effective rotational velocity of the blade when is located about 135° in the rotation direction from the top.

10. Forces and moments on appendages

Direct integration of the forces and moments in the ship system of coordinates was performed for propellers, rudders blades and roots, bilge keels, propeller shafts, and shaft supporting struts. Each of these corresponds to a component designed to exert thrust (propellers), to control roll and enhance stability (bilge keels and rudder roots), or needed due structural and mechanical requirements (shafts and struts). Proper design requires good ability to perform the required task, while minimizing undesired effects. The surge force and roll and yaw moments are shown in Figs. 13–15, respectively.

The surge force shows that resistance from the appendages is moderate during the early stage of the broaching event, where the ship is drifting and rolling moderately, defined perhaps by the first 3 s of the run, see Fig. 3. As already discussed, in this stage the propellers' thrust is biased a bit to port but essentially balanced. The rudders have acted little, and thus their resistance is limited to about 1 N. Beyond the initial transient, the bilge keels show a significant imbalance with the port side showing a resistance of about 0.75 N while the starboard bilge keel experiences 0.3 N. The contribution of the rudders and bilge keels to the total resistance in this stage is approximately 6.5%, a considerable number. The rudder roots develop very small resistance at all times, showing their good design and alignment with the flow. The shafts
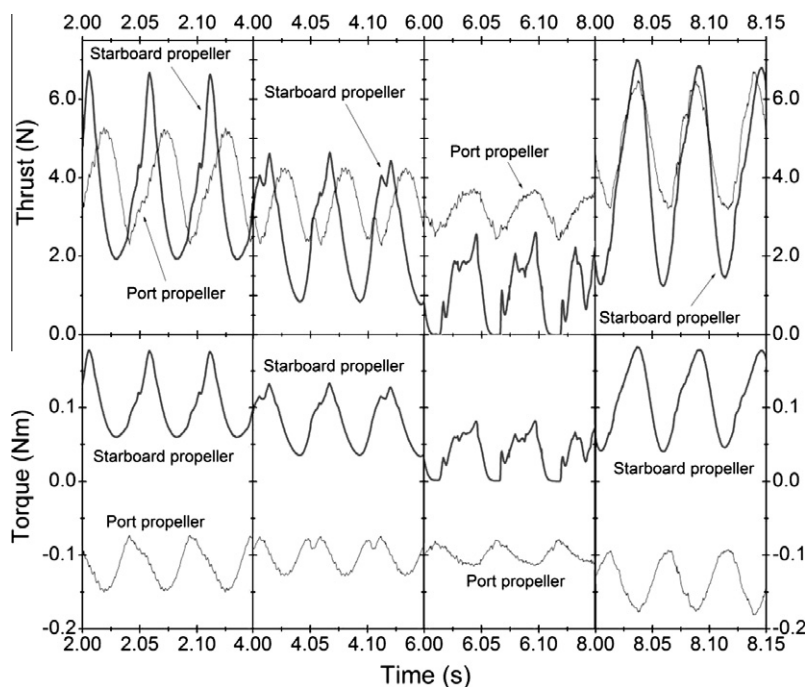
to a very uniform inflow, resulting in fluctuation amplitudes of only 1 N and 0.4 Nm for thrust and torque, respectively. At 8 s, when the ship is getting back upright after the roll excursion ends, the ship velocity has decreased considerably (Fr = 0.34, see Fig. 3), and the load on the propellers is very large. The starboard propeller blade exhibits peak-to-peak fluctuation in excess of 5 N, with maximum thrust and torque comparable to those of the port propeller, but considerably lower minimum values as the blade approaches the free surface.

Frequency spectra of the blade thrust for four different 1 s intervals for Case 1 are shown in Fig. 12. Recall that the time step of the computation is $\Delta t = 0.00025$, corresponding to a dimensional time step of 0.283 ms, enough to resolve frequencies in the order of the kHz. Since the integration period for each FFT is 1 s, clipping prevents resolution of frequencies lower than about 10 Hz. As

Fig. 10. Thrust and torque experienced by a single blade at different times for Case 1.
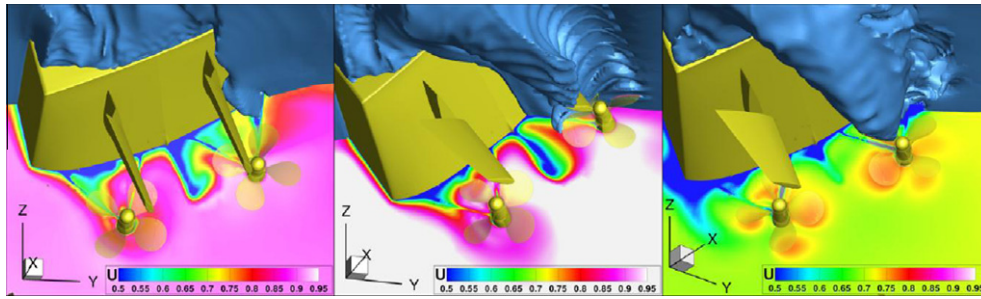
Fig. 11. Axial velocity in the ship system of reference upstream of the propellers and downstream of the struts at 4 s (left), 6 s (center), and 8 s (right) for Case 1.
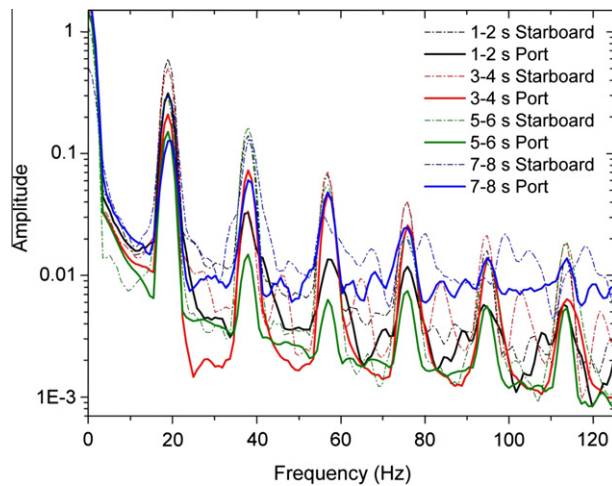

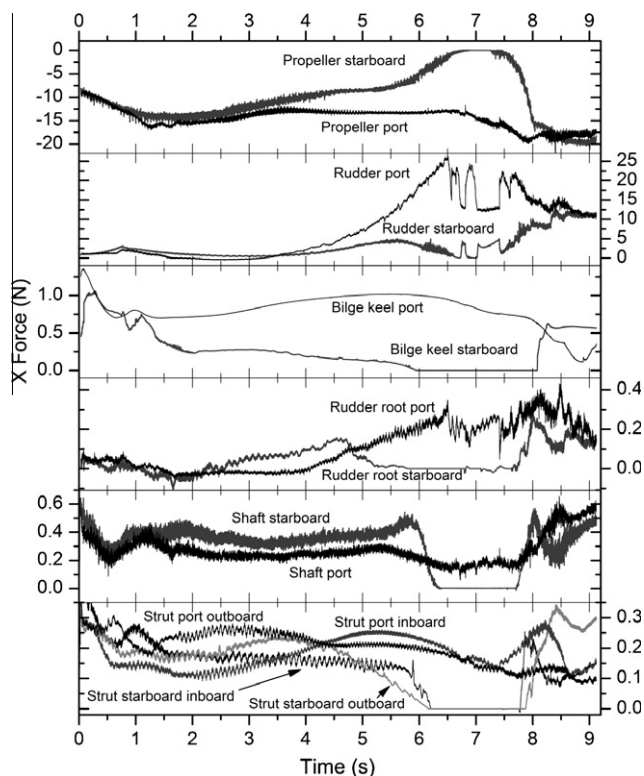**Fig. 12.** Frequency spectra of the blade thrust at four different 1 s intervals for Case 1.

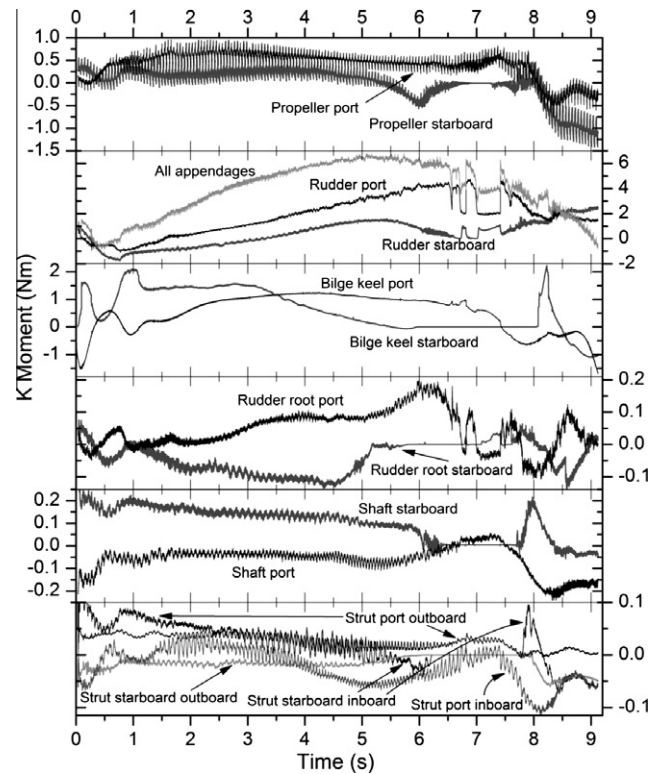**Fig. 13.** Surge force on different appendages for Case 1.

Fig. 14. Roll moment on different appendages for Case 1.

show more resistance on the starboard side, totaling about 0.6 N between both sides, while the struts present a total resistance in the order of 0.7 N, with the outboard struts contributing more than the inboard ones, probably due to poor alignment with the flow. Shafts and struts contribute another 3% to the total resistance.

During the later stage of the broaching event and recovery (3–9 s), the starboard propeller and rudder come out of the water, and their contribution to thrust and resistance decline considerably. The rudders turn all the way to port, and thus the port rudder resistance increases dramatically, to completely overcome the propeller thrust. At this point the ship speed decreases considerably and the roll excursion is at its maximum, while the yaw rate and drift angle also peak (see Fig. 3). This situation presents very instable free surface waves that hit the rudders, or reduce their wetted surface area in the case of the port rudder (see the animation in Electronic Annex I), causing strong fluctuations on the forces and moments on the rudders. After the ship recovers from the roll excursion the propeller thrust and rudder resistance become more balanced between port and starboard sides, with a considerable decline in rudder resistance. The difference in resistance for the port and starboard bilge keels increases as the roll angle increases,
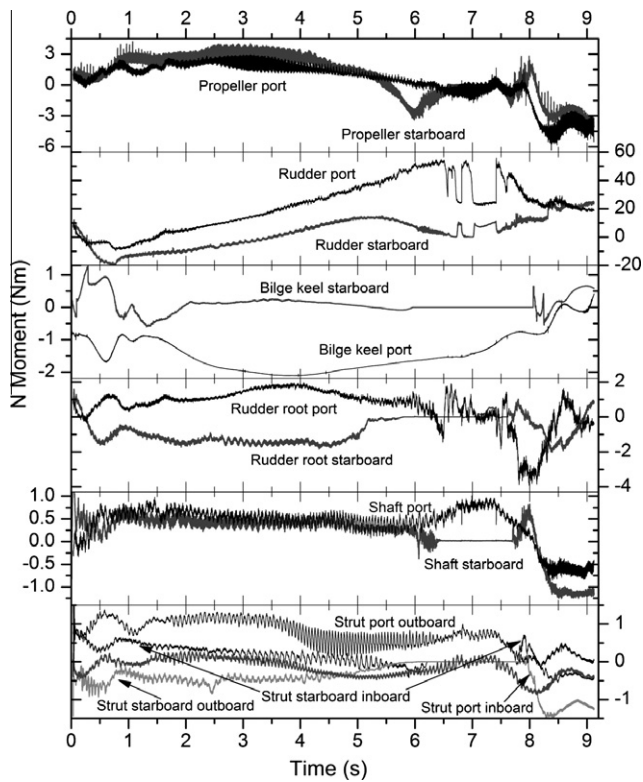
Fig. 15. Yaw moment on different appendages for Case 1.

with the starboard bilge keel completely out of the water for a roll angle of 40° and the port bilge keel reaching a resistance of 1 N. The port rudder root shows increasing resistance as the port rudder turns more to port, peaking at about 0.35 N. The starboard shaft resistance is larger than the port side resistance, likely because it is subject to higher velocity, see Fig. 11. Of course as the starboard shaft gets out of the water its resistance decreases to zero. The inboard struts show similar behavior, while the outboard struts show the opposite, with the port strut exerting more resistance. This is possible due to the proximity of the starboard to the free surface even at moderate roll angles (it starts coming out of the water at about 15° of roll).

Analysis of the roll moments displayed in Fig. 14 is revealing, showing most appendages contributing to a net roll moment to port. The port propeller creates a positive roll moment (to port) of about 0.5 Nm, while the starboard propeller is essentially neutral. The rudders also contribute with a positive roll moment, as discussed earlier, that combined reach up to 5 Nm. The bilge keels resist drift velocities, and thus contribute with a positive roll moment of up to 2.5 Nm, mostly on the first stage of the simulation, and the roll moment remains positive until the roll rate changes sign at about 7.5 s. The port and starboard rudder roots are mostly balanced, with the exception of the time when the starboard root gets out of the water, when the net rolling moment is positive but small for a while. The shafts show a net positive roll moment, with the port shaft slightly negative. The net small positive roll moment is due to the average cross flow from port to starboard caused by the drift of the ship. The struts behave similarly, though the net moments are smaller. Overall, the net roll moment for all appendages reaches in excess of 6 Nm, a value that is balanced by the static righting moment achieved at 70° of roll [8].

The yaw moments, Fig. 15, show that the turning moments produced by the appendages are dominated by the rudders, with values one order of magnitude larger than any other appendage. Interestingly, both propellers contribute a net positive turning

moment (to port), helping prevent broaching. It is striking how ineffective the starboard rudder is compared to the port rudder, even when it still in water. A redesign of the rudders to work better under high rolling and drifting conditions could improve greatly the safe operational envelope of this ship. Though small compared with the rudders, the bilge keels contribute a net turning moment to port, also hampering the work of the rudders. Contributions from shafts, though small, are of positive yaw moment, as are in average those of the rudder roots. The struts net yaw moment is very small.

Some appendages experience significant forces and moments oscillations of relatively low frequency. Particularly strong are those from the shafts and struts, but also oscillations are present in all appendages except the bilge keels. These oscillations are due to local flow instabilities in the appendages, but also due to unsteady flow hitting the appendages. Particular cases of this are the rudders, which are subject to highly unsteady flow from the propellers, separation from the struts and shaft, and free surface instabilities. Fig. 16 shows the frequency spectra of the whole time history of the surge force on appendages on the port side. Notice that the main frequency present in most appendages is about 76 Hz, corresponding to the blade passage frequency or 4 times the rotational frequency for a four-bladed propeller. The inboard strut shows also a wider peak at much lower frequency, approximately 14 Hz and extending up to 20 Hz, corresponding to several vortex shedding frequencies throughout the run. The outboard strut also shows a peak around 14 Hz and a wide response up to 20 Hz, but other low frequencies are present with smaller amplitude, notably around 8 Hz and 3.5 Hz. The shaft shows high amplitude at frequencies similar to the outboard strut, but a clear peak around 3.5 Hz is present with much more amplitude than the outboard strut. This peak is also present in the bilge keel, but with much less amplitude. An animation showing the vortices represented by isosurfaces of $Q = 500$ is included in Electronic Annex IV (with time slowed to 15% of the real frame rate), where the vortex shedding from the shafts is clear. Fig. 17 shows a still image at 5.66 s depicting the main vortices induced by the appendages.

The propeller has a very large amplitude peak at the blade passage frequency, as expected, and responds with much lower amplitude to the frequencies present in the forces in shafts and struts. Higher harmonics of these frequencies are also present. It is interesting to note that the rudder reacts much strongly to low frequencies than to high frequencies, barely responding to the propeller blade passage frequency and the reaction of the propeller to the
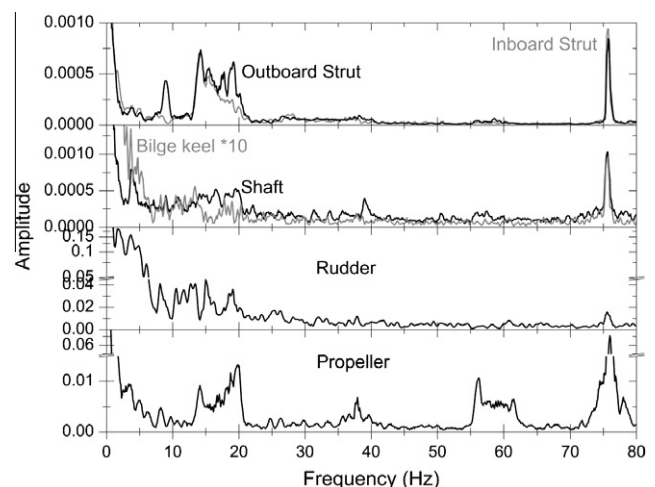

Fig. 16. Frequency spectra of the surge force of different port side appendages for Case 1.
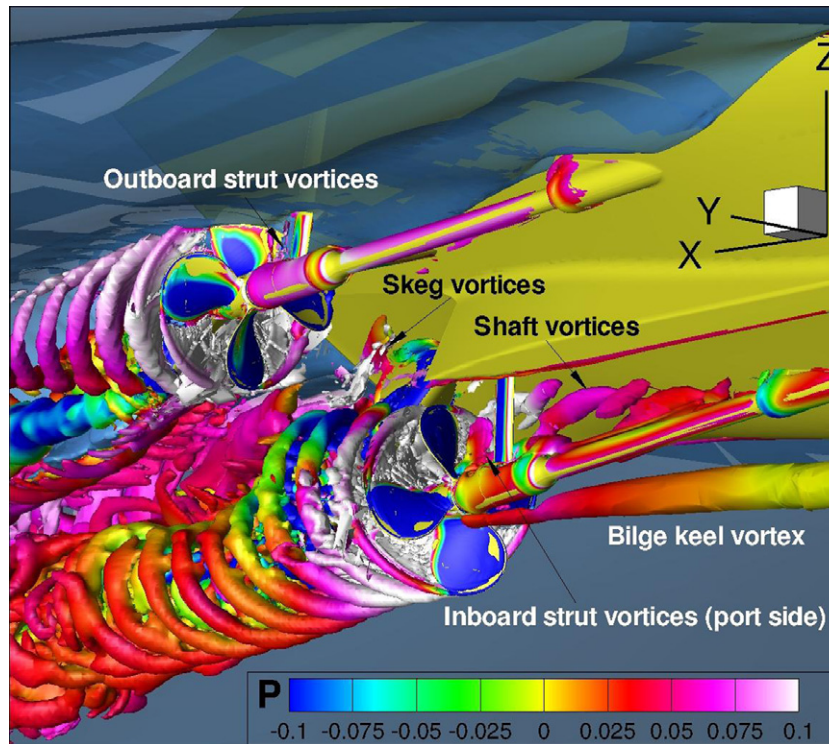
Fig. 17. Main vortices shed by the appendages at 5.66 s for Case 1.

shaft and strut vortices. On the other hand, very large responses at 2 Hz and 3.5 Hz are evident. The first frequency is associated with the waves hitting the rudders during the period lasting approximately from 6.5 s to 7.5 s, while the second is probably caused by free surface instabilities in the stern area.

11. Results with a PI controller

The case exposed here presents an opportunity to evaluate options to improve the safe operating envelope range of the ship. Since two broaching conditions are identified, design changes can be attempted to prevent broaching on these, instead of resorting to more costly probabilistic methodologies. In view of the analysis of the broaching processes of Case 1 and Case 2, only the simplest design alternative is evaluated here, which is to change the logic of the autopilot controller so the rudders act faster before the ship heading respect to the waves causes unmanageably high wave-induced yaw moments. Other possibilities could include geometry changes, like larger or redesigned rudders to increase the turning moment while reducing the induced rolling moment, reposition the bilge keels further aft to induce a positive yaw moment and help the rudders, or any other mechanism that will help steer the ship while reducing the roll angle. Only the conditions of Case 1 are used, because is a milder case than Case 2 and it is thus easier to prevent broaching with simple changes.

Case 3 is then identical to Case 1, but the proportional controller is replaced at $t = 3$ s by a variable gain proportional–integral controller. This is done by restarting the case with a new set of PI constants, starting at $P = 5$ and decreasing this value to a minimum of $P = 3$ at $t = 7.5$ s. The integral constant is found such that the overall rudder action is continuous between changes of parameters, which was done once every half a second. This resulted in integral values varying between 2 and 0.75. This very simple controller has the effect of forcing the rudders considerably more at the beginning of the broaching event, when the heading error is still small but the

yaw rate is already considerable, see Fig. 3. Under milder conditions this large controller gain could result in unstable behavior, but at Froude numbers in excess 0.4 there is plenty of dynamic damping forces to stabilize the ship.

Discussion is based on Fig. 3 and Electronic Annex V, which shows an animation of Case 3 slowed to 50% the frame rate of the real process. Notice that as soon as the controller parameters are changed, the ship reverses the high yaw rate to port that characterizes Cases 1 and 2. To achieve the correction the rudders go hard to port in about 2 s, limiting the roll excursion to less than 25°. The ship then undergoes an accommodation into a surf riding condition, with the rudders balancing at about 8° to port and drift angle of less than 1°. At the end of the computation the final steady state has not been achieved, though the ship is running smoothly toward it. After a nose-diving of over −4° of pitch the bow is accommodating upward as the ship slowly stabilizes in the trough of the wave. The ship speed has not reached its steady state speed of $Fr = 0.483$, but decreasing toward it after reaching a peak speed of $Fr = 0.525$. At this condition the equilibrium roll angle is about 10°.

A time sequence of Cases 1 and 3 is shown in Fig. 18. From the beginning of the run until the third frame the controller is proportional with unit gain for both cases. At that time Case 3 switches to a proportional–integral controller, preventing the broaching event as discussed above. At the time of the switch the ship is still controllable, in the sense that swift operation of the rudders can restore steering ability. There is, however, a point in which the roll angle and direction to the waves create a yaw moment that cannot be overcome with the maximum rudder turning moment. A good captain or autopilot should always act well before the ship reaches this point, and the best way to do this is to have an algorithm that can use information of the waves to come to position the ship in such a way that the yaw moment broadside to the waves is minimized. This, of course, requires in-advance knowledge of the waves, which can possibly be obtained from radar information several minutes before the waves hit the ship [22]. Combination of
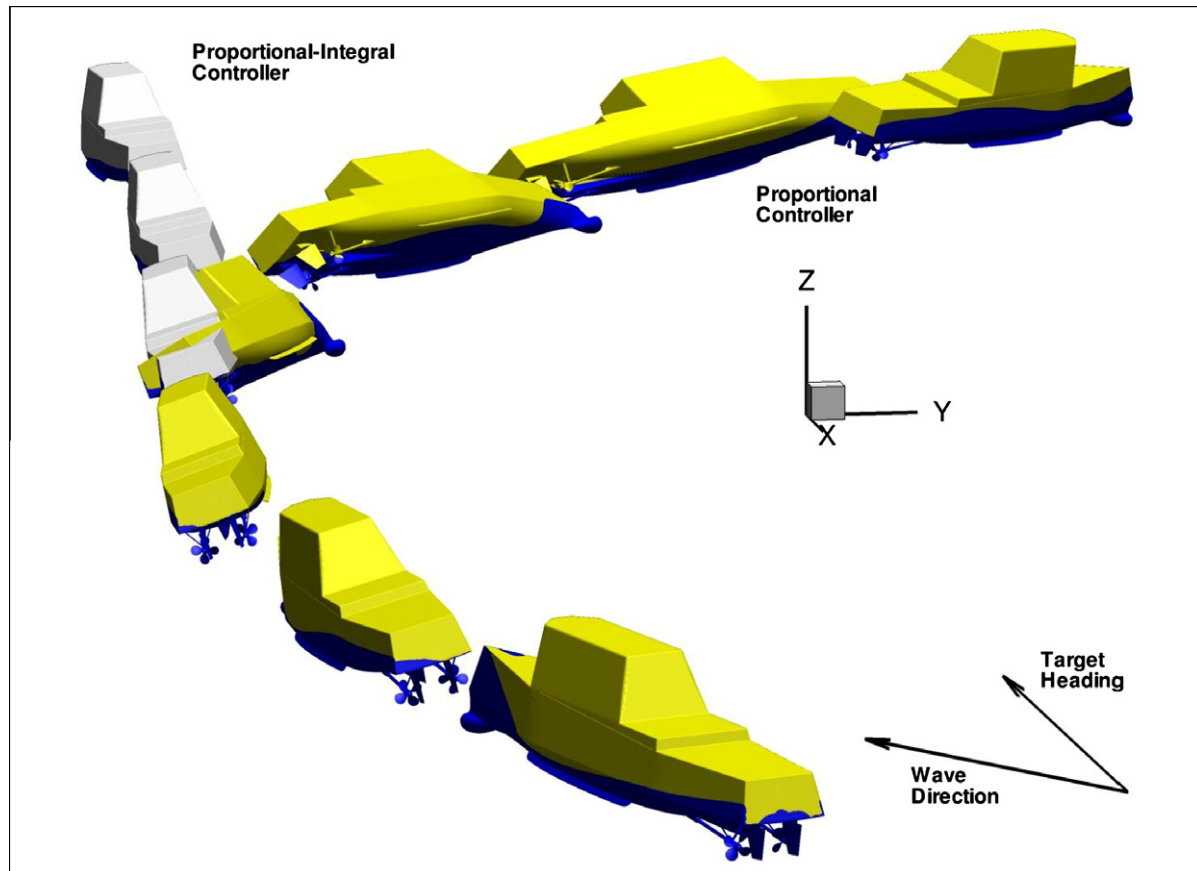
Fig. 18. Trajectories for Cases 1 and 3.

predictive controllers with on-board radar data could provide ships in extreme environmental conditions a way to safely maneuver through the waves.

12. Conclusions and future work

Broaching of the fully appended ONR Tumblehome model DTMB 5613 in following regular waves was simulated for two conditions. These conditions are used to validate the simulations against experimental data and to analyze the broaching process, through study of the flow field and forces and moments on the hull and individual appendages. It is found that better dynamic stability to roll and improved steering could be achieved by reducing the rolling moment caused by the rudders, and by improving the positioning of the bilge keels. The use of a slightly better autopilot prevents broaching under identical operating conditions to those previously causing broaching. In the area of control a great opportunity exists to extend the safe operating envelope, where a fairly primitive heading controller performs significantly better than the overly simplistic proportional controller. In addition to designing the vessel for dynamic stability and continued steering ability under adverse conditions, an advanced predictive controller that accounts for wave information could dramatically improve the range of operation of the ship, at the same time providing a more comfortable navigation.

Future work will be focused on the study of controllers to extend the safe operating envelope, a verification study to gain confidence on the CFD predictive capabilities as previously discussed in section "Validation," and on implementation of advanced propeller inviscid solvers to reduce the cost of the computations by an order of magnitude. Advanced propeller solvers such as PUF-14 [34] or PUF3A interact with the CFD code through body forces and can add effects such as cavitation and ventilation through simpler modeling than in direct CFD computations. Work is under way to couple the code PUF-14 with CFDShip-Iowa V4.5.

Acknowledgments

Appendix A. Supplementary data

Supplementary data associated with this article can be found, in the online version, at doi:10.1016/j.compfluid.2011.10.002.

References

[1] Belenky VL, Weems KM, Lin WM. Numerical procedure for evaluation of capsizing probability with split time method. In: Proceedings of the 27th symposium on naval hydrodynamics, Seoul, Korea; 2008.
[2] Bhushan S, Xing T, Carrica PM, Stern F. Model- and full-scale URANS simulations of Athena resistance, powering, seakeeping, and 5415 maneuvering. J Ship Res 2009;53:179–98.
[3] Boger DA, Dreyer JJ. Prediction of hydrodynamic forces and moments for underwater vehicles using overset grids. In: AIAA paper 2006-1148. 44th AIAA Aerospace Sciences Meeting, Reno, NV, USA; 2006.
[4] Bugalski T, Hoffman, P. Numerical simulation of the interaction between ship hull and rotating propeller. In: CFD workshop Gothenburg 2010, Gothenburg, Sweden; 2010.
[5] Califano A, Steen S. Analysis of different propeller ventilation mechanisms by means of RANS simulations. In: First int symp marine propulsors, Trondheim Norway; 2009.

[6] Carrica PM, Wilson R, Stern F. An unsteady single-phase level set method for viscous free surface flows. Int J Numer Meth Fluids 2007;53:229–56.

[7] Carrica PM, Wilson RV, Noack R, Stern F. Ship motions using single-phase level set with dynamic overset grids. Comput Fluids 2007;36:1415–33.

[8] Carrica PM, Paik K, Hosseini H, Stern F. URANS analysis of a broaching event in irregular quartering seas. J Mar Sci Technol 2008;13:395–407.

[9] Carrica PM, Stern F. DES simulations of KVLCC1 in turn and zigzag maneuvers with moving propeller and rudder. in: SIMMAN 2008, Copenhagen, Denmark; 2008.

[10] Carrica PM, Castro AM, Stern F. Self-propulsion computations using speed controller and discretized propeller with dynamic overset grids. J Mar Sci Technol 2010;15:316–30.

[11] Carrica PM, Huang J, Noack R, Kaushik D, Smith B, Stern F. Large-scale DES computations of the forward speed diffraction and pitch and heave problems for a surface combatant. Comput Fluids 2010;39:1095–111.

[12] Carrica PM, Fu H, Stern F. Computations of self-propulsion free to sink and trim and of motions in head waves of the KRISO Container Ship (KCS) model. Appl Ocean Res 2011;4:309–20.

[13] Castro AM, Carrica PM, Stern F. Full scale self-propulsion computations using discretized propeller for the KRISO Container Ship KCS. Comput Fluids 2011;51:35–47.

[14] Celik I, Klein M, Freitag M, Janicka J. Assessment measures for URANS/DES/LES: an overview with applications. J Turbulence 2006;7:1–27.

[15] Celik I, Klein M, Janicka J. Assessment measures for LES applications. J Fluids Eng 2009;131:031102.

[16] Fossen TI. Guidance and control of ocean vehicles. New York: Wiley; 1994.

[17] Greve M, Abdel-Maksoud M, Eder S, De Causmaecker. Steady viscous flow calculation around the KCS model with and without propeller under consideration of the free-surface. In: CFD workshop Gothenburg 2010, Gothenburg, Sweden; 2010.

[18] Huang J, Carrica P, Stern F. Semi-coupled air/water immersed boundary approach for curvilinear dynamic overset grids with application to ship hydrodynamics. Int J Numer Meth Fluids 2008;58:591–624.

[19] Jin W, Gao Q, Vassalos D. The prediction of KCS resistance and self-propulsion by RANSE. In: CFD workshop Gothenburg 2010, Gothenburg, Sweden; 2010.

[20] Lee JH, Rhee SH. Flexible CFD meshing strategy for prediction of ship resistance and propulsion performance. In: CFD workshop Gothenburg 2010, Gothenburg, Sweden; 2010.

[21] Lübke LO. Numerical simulation of the flow around the propelled KCS. In: CFDWS05, Tokyo, Japan; 2005.

[22] Lyzenga D, Nwogu O. Shipboard radar measurements of ocean waves for real-time prediction of nonlinear ship motions. In: Proc 28th symp naval hydrodynamics, Pasadena, CA; 2010.

[23] Menter FR. Two-equation eddy viscosity turbulence models for engineering applications. AIAA J 1994;32:1598–605.

[24] Mousaviraad MS, Carrica P, Stern F. Development and validation of harmonic wave group single-run procedure for RAO with comparison to regular wave and transient wave group procedures using URANS. Ocean Eng 2010;37:653–66.

[25] Noack R. Suggar: a general capability for moving body overset grid assembly. In: AIAA paper 2005-5117. 17th AIAA computational fluid dynamics conf., Toronto, ON, Canada; 2005.

[26] Pankajakshan R, Remotigue S, Taylor L, Jiang M, Briley W, Whitfield D. Validation of control-surface induced submarine maneuvering simulations using UNCLE. In: Proc 24th symp naval hydrodynamics, Fukuoka, Japan; 2004.

[27] Sadat-Hosseini H, Carrica PM, Stern F, Umeda N, Hashimoto H, Yamamura S, et al. CFD, system-based and EFD study of ship dynamic instability events: surf riding, periodic motion and broaching. Ocean Eng 2011;38:88–110.

[28] Spyrou KJ. Dynamic stability in quartering seas – Part III. Non-linear effects on periodic motions. J Ship Res 1997;41:210–33.

[29] Stern F, Kim HT, Patel VC, Chen HC. A viscous-flow approach to the computation of propeller–hull interaction. J Ship Res 1988;32:246–62.

[30] Travin A, Shur M, Strelets M, Spalart PR. Physical and numerical upgrades in the detached-eddy simulation of complex turbulent flows. In: Friedrich R, Rodi W, editors. Advances in LES of complex flows. Kluwer Academic Publishers; 2002.

[31] Umeda N, Maki A, Hashimoto H. Manoeuvring and control of a high-speed slender vessel with twin screws and twin rudders in following and quartering seas. J Japan Soc Naval Arch Ocean Eng 2006;4:155–64 [in Japanese].

[32] Umeda N, Matsuda A, Hashimoto H, Yamamura S, Maki A. Model experiments on extreme motions of a wave-piercing tumblehome vessel in following and quartering waves. J Japan Soc Naval Arch Ocean Eng 2008;8:123–9.

[33] Venkatesan G, Clark W. Submarine maneuvering simulations of ONR body 1. In: Proc OMAE2007, San Diego, CA; 2007.

[34] Warren CL, Taylor TE, Kerwin JE. A coupled viscous/potential-flow method for the prediction of propeller-induced maneuvering forces. In: SNAME propellers/shafting symp., Virginia Beach, VA; 2000.

[35] Wu Q, Feng XM, Yu H, Wang JB, Cai RQ, Chen XL. Prediction of ship resistance and propulsion performance using multi-block structured grids. In: CFD workshop Gothenburg 2010, Gothenburg, Sweden; 2010.

[36] Xing T, Kandasamy M, Stern F. Unsteady free-surface wave-induced separation: analysis of turbulent structures using detached eddy simulation and single-phase level set method. J Turbulence 2007;8:1–35.

[37] Yamamura S, Maki A, Umeda N, Sano H. Numerical study towards physics-based criteria for avoiding broaching and capsizing in following/quartering waves. In: International workshop on dynamic stability considerations in ship design, Ilawa, Poland; 2009.